Vacancy-Driven Stabilization of Sub-Stoichiometric Aluminate Spinel High Entropy Oxides

Christopher Riley,* Nichole Valdez, Christopher M. Smyth, Richard Grant, Brandon Burnside, James Eujin Park, Stephen Meserole, Angelica Benavidez, Robert Craig, Stephen Porter, Andrew DeLaRiva, Abhaya Datye, Mark Rodriguez, and Stanley S. Chou
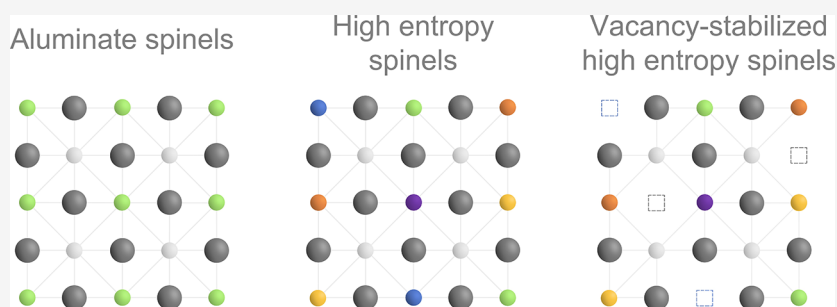
Read Online

ACCESS | Metrics & More | Article Recommendations | SI Supporting Information

ABSTRACT: Despite significant recent developments in the field of high entropy oxides, previously reported HEOs are overwhelmingly stoichiometric structures containing a single cationic site and are stabilized solely by intermixing increasing numbers of cations. For the first time, we demonstrate here that cationic vacancies can significantly increase configurational entropy and stabilize phase-pure HEOs. Aluminate spinel HEOs with AB_2O_4 stoichiometry are used as a model crystal structure. These spinels tolerate large divalent cation deficiencies without changing phase, allowing for high concentrations of cationic vacancies. Stoichiometric and sub-stoichiometric spinels (with A:B molar ratios <0.5), which contained various mixtures of Co, Cu, Mg, Mn, Ni, and cationic vacancies in nominal equimolar concentration, were systematically compared as a function of heat treatment temperature and number of unique cationic species. We found that the same number of cationic species were needed to stabilize both stoichiometric and sub-stoichiometric nickel-containing spinels at 800 °C calcination, as exemplified by $(CoCuMgNi)Al_2O_4$ and $(CoMgNi)_{0.75}Al_2O_x$ samples, signifying that vacancies stabilize phase-pure spinels similarly to cations. The chromatic, structural, and chemical properties of these complex spinels were highly tunable via incorporation of cationic vacancies and multiple divalent metals, promoting their potential application as unique pigments, catalysts, and thermal coatings.
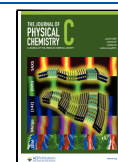
INTRODUCTION

High entropy oxides (HEOs) are a relatively new class of materials containing multiple cations (typically four or more) consolidated into a single-phase crystal structure. These structures are stabilized through configurational entropy (S_c), which increases with the number of unique arrangements of cations and anions within the crystal structure according to eq 1.[1] X_i and y_j are mole fractions of each cationic and anionic species, respectively, and N and M are the total number of unique cationic and anionic species, respectively. For a given value of N and M, S_c is maximized when the species are in equimolar concentration. The tendency of the constituent cations to adopt dissimilar secondary oxide phases is overcome when increased entropy outweighs enthalpic energy penalties associated with mixing, according to the Gibbs equation ($\Delta G = \Delta H - T\Delta S$). High entropy oxides that exhibit this thermodynamic phenomenon are further distinguished as entropy-stabilized oxides. Previous studies report HEOs

adopting a variety of different crystal structures, including rock salt,[1,2] fluorite,[3−5] spinel,[6−8] and perovskite,[9−11] which have demonstrated advantageous ionic conductivity,[12] thermal conductivity,[9] dielectric constants,[13] and catalytic properties.[14−16] These oxides were stabilized solely by increasing the number of cationic elements mixed together and increasing the temperature until a phase-pure structure formed. Despite the recent development of complex perovskite and transition metal spinel HEOs,[6,17,18] many of these studies focused on stoichiometric crystal structures having a single equivalent

cationic site, an approach that ultimately limits the number of parameters available to design unique complex oxides.

$$S_c = -k_B \left[\left(\sum_{i=1}^{N} x_i \ln(x_i) \right)_{\text{cation}} + \left(\sum_{j=1}^{M} y_j \ln(y_j) \right)_{\text{anion}} \right] \quad (1)$$

The aim of this current study is to evaluate the potential of cationic vacancies to stabilize HEOs. From a configurational entropy perspective, site vacancies constitute a unique chemical species that increases the number of unique atomic configurations within a crystal lattice in the same manner as a cation.[19,20] Unfortunately, most metal oxide crystal structures do not support large vacancy concentrations, which prevents their systematic study. Aliovalent cation dopant incorporation and oxygen partial pressure change are shown to induce vacancies in both compositionally simple and high entropy oxides.[8,12,15,21,22] However, vacancy concentrations induced through these methods are typically too low to significantly increase configurational entropy.[23,24] Since crystallographic defects enhance many of the useful properties of metal oxides (ionic conductivity, energy storage, and catalytic activity for instance),[15,25,26] a systematic study of defect-stabilized HEOs would be valuable. Further, cationic vacancies are accompanied by charge-compensating anionic vacancies, enabling a configurational entropy contribution from the anionic sub-lattice, which is typically assumed to be zero in metal oxides.[27,28] High entropy carbides,[29,30] silicides,[31,32] borides,[33–35] and sulfides[36–38] offer an alternative to oxygen anions in compositionally complex materials. Several studies of high entropy carbides demonstrate significant anionic vacancy concentrations shown to stabilize the carbide structure, which suggests the same principle may stabilize other material systems, like metal oxides.[39,40] However, a method for supporting high vacancy concentrations is lacking in previously studied HEOs.

Here, we develop HEOs having an aluminate spinel crystal structure. These are AB_2O_4 type oxides in which A-site cations have tetrahedral coordination and B-site cations have octahedral coordination. Stoichiometric aluminate spinels have MAl_2O_4 composition, where M is a divalent cation. However, previous studies observed that aluminates with divalent cation concentrations significantly below stoichiometric values retained a spinel crystal structure by accommodating cationic site vacancies and charge-compensating oxygen vacancies.[41–43] In fact, γ-alumina, a common Al_2O_3 phase having no divalent cations, adopts a defected spinel structure containing site vacancies.[44,45] Thus, these materials are uniquely suited for a systematic study of vacancy-contributed configurational entropy. The presence of two cationic sub-lattices also enables site inversion, a unique structural feature that can increase configurational entropy.[46,47] Inversion occurs when divalent cations occupy octahedral sites instead of tetrahedral, and trivalent cations occupy tetrahedral sites instead of octahedral. The inversion parameter describes the extent to which this phenomenon occurs and is given as x in the formula $(A_{1-x}B_x)(B_{2-x}A_x)O_4$ for stoichiometric spinels, where $x = 0$ in normal spinels and $x = 1$ in fully inverse spinels. Although Al^{3+} ions prefer octahedral coordination, the energetics of the divalent cations often dictate site occupation of both cations within a spinel structure.[48,49] Ni^{2+} and Cu^{2+} energetically favor octahedral site occupation and form inverse aluminate spinels, but $CuAl_2O_4$ with a highly disordered normal spinel structure has also been observed.[50] On the other hand, Mn^{2+} and Co^{2+}

show little energetic preference, and Mg^{2+} favor tetrahedral sites.[48] Accounting for site vacancies and cation inversion, a formula for configurational entropy for non-stoichiometric spinels is given as eq 2. Non-zero configurational entropy contribution from two cationic sub-lattices and an anionic sub-lattice clearly offers a unique opportunity to study entropic stabilization within complex spinels, which is inaccessible in many previously studied HEO materials.

$$S_c = -k_B \left[\left(\sum_{i=1}^{N} x_i \ln(x_i) \right)_{\substack{A-\text{site} \\ \text{cation}}} + \left(\sum_{i=1}^{N} x_i \ln(x_i) \right)_{\substack{B-\text{site} \\ \text{cation}}} \right.$$
$$\left. + \left(\sum_{j=1}^{M} y_j \ln(y_j) \right)_{\text{anion}} \right] \quad (2)$$

Herein, aluminate spinels were produced with increasing numbers of divalent cationic species, including Co, Cu, Mg, Mn, and Ni ions and cationic vacancies in varying combinations. Cationic vacancies were induced by using metal precursors with M^{2+}/Al^{3+} ratios <0.5 in a facile sol−gel synthesis. Stoichiometric and sub-stoichiometric samples containing one to five cationic species were systematically heated from 800 to 950 °C and measured for phase purity. Sample XRD patterns were compared to those generated from modeled spinel crystal structures to determine the average cationic site occupation and vacancy concentration, similar to methods reported in previous literature.[47,51] Due to the relatively high energetic barrier for $NiAl_2O_4$ formation, we focused primarily on spinels containing Ni. We further evaluated the samples for chromatic, chemical, and thermal properties, which are relevant to the primary applications of aluminate spinels as aesthetic pigments,[52,53] catalysts,[42] and refractory materials.[54] We demonstrate that these properties are highly tunable through the inclusion of both multiple divalent cations and cationic vacancies, as compared to simple spinels.

■ EXPERIMENTAL METHODS

Spinel samples were synthesized through a sol−gel synthesis previously reported with several adjustments.[15,55,56] First, 5 g of polyvinylpyrrolidone (Aldrich, 40,000 average MW) were dissolved in 100 mL of DI water under vigorous stirring. Metal nitrate precursors were then added to the polymer solution and stirred for 1 h. 14 mmol of aluminum (III) nitrate nonahydrate (Sigma-Aldrich, ≥98%, ACS reagent) were added. A total of 7 mmol of divalent metal nitrates were added to make stoichiometric spinels or <7 mmol for sub-stoichiometric spinels. Divalent metal precursors included cobalt (II) nitrate hexahydrate (Sigma-Aldrich, 98%), copper (II) nitrate hemipentahydrate (Sigma-Aldrich, ≥99.99% trace metals basis), magnesium (II) nitrate (Sigma-Aldrich, ACS reagent 99%), manganese (II) nitrate tetrahydrate (Alfa Aesar, 98%), and nickel (II) nitrate hexahydrate (Alfa Aesar, 99.9985% metals basis). The resulting solutions were heated at 110 °C overnight to evaporate water and form hard gels. These gels were crushed to a coarse powder and placed in the center of a vented box furnace preheated at 800 °C for 2 h to calcine within a fume hood. One set of samples was subjected to the same calcination parameters but with ramp rates of 5 and 25 °C/min to evaluate this effect on phase purity. Calcined samples containing
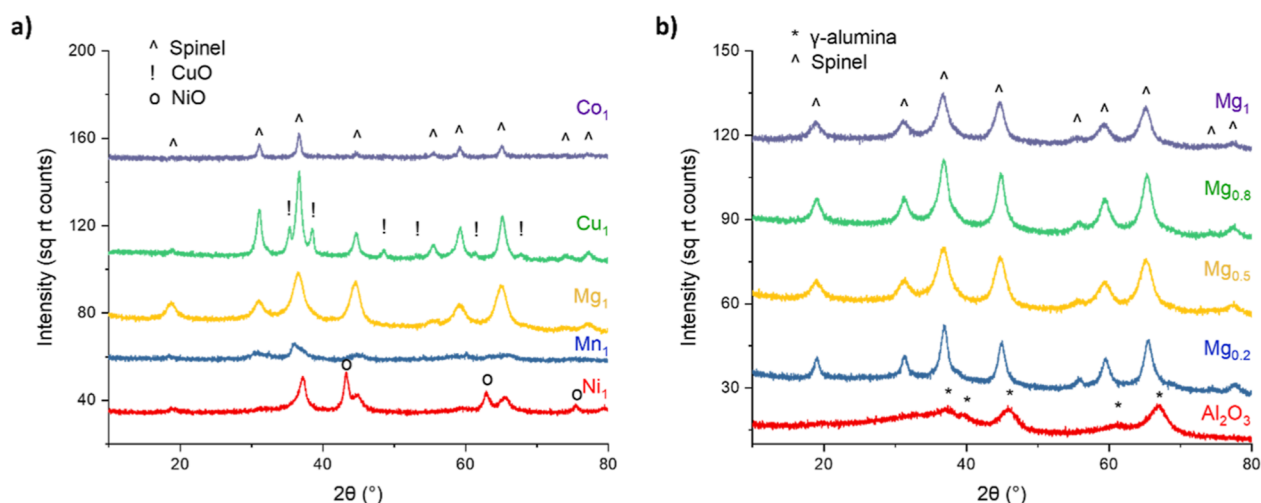
Figure 1. XRD patterns of (a) stoichiometric simple spinels and (b) alumina and magnesium aluminates with varying Mg stoichiometry, all calcined at 800 °C.

secondary oxide phases were further heated at temperatures between 850 and 950 °C for 2 h followed by quenching in ambient air to demonstrate the effect of temperature on phase-pure spinel formation. For simplicity, spinel samples are labeled according to the constituent divalent metals and their nominal concentration. Parentheses are used to designate equimolar concentrations of the enclosed elements, which are listed in alphabetical order. For instance, stoichiometric spinel containing only nickel is labeled Ni_1, and stoichiometric spinel containing both nickel and magnesium is labeled $(NiMg)_1$. Sub-stoichiometric spinels are labeled with A-site cation stoichiometry values less than 1, such as for the sample having equimolar concentrations of nickel, magnesium, and cationic vacancies labeled as $(NiMg)_{0.67}$, wherein one-third of A-sites are assumed to be vacant. Where appropriate, the samples are also labeled with the highest heat treatment temperature used to compare the effect of aging on single phase formation. Otherwise, samples labeled without a temperature underwent 800 °C calcination as the sole heat treatment.

Electron probe microanalysis (EPMA), X-ray diffraction (XRD), X-ray fluorescence (XRF), scanning electron microscopy (SEM), Raman spectroscopy, transmission electron microscopy (TEM), X-ray photoelectron spectroscopy (XPS), and diffuse reflectance spectroscopy (DRS) characterization was conducted to verify sample composition, identify the crystalline phases present, and analyze the chromatic properties. EPMA analysis measured the sample elemental composition and was conducted using a JEOL JXA-8530F HyperProbe on pelletized and carbon-coated samples. XRF compositional analysis was performed with a Bruker M4 Tornado micro-XRF instrument using a Rh X-ray source operated at 50 kV and 0.2 mA. Sample data were compared against a calibration curve of metal oxide standards. BET specific surface area measurements were taken with a Micromeritics Gemini 2360 Surface Area Analyzer. The samples were outgassed overnight at 120 °C in flowing nitrogen prior to analysis. XRD patterns were collected with a Bruker D2Phaser diffractometer equipped with a LYNXEYE XE-T linear detector operating with Bragg–Brentano geometry and Cu Kα radiation. The samples were analyzed using a 0.02° step size and approximately 5°/min scan rate. Patterns were analyzed through Rietveld refinement with JadePro version 8.7 XRD analysis software to identify the crystalline phases and their

respective lattice parameters and average crystallite sizes. Rietveld refinement was further used to model the relative site occupation of aluminum, divalent cations, and site vacancies within select spinel samples; divalent cations coexisting in HEO samples were modeled as a single element having equivalent electron density as the average of the divalent cations. For these models, the XRD patterns were collected with a Siemens θ–θ D500 diffractometer equipped with a sealed-tube Cu anode X-ray source, diffracted beam graphite monochromator, and scintillation detector. Images and elemental maps were generated via SEM energy dispersive spectroscopy (EDS). A Zeiss Supra 55VP microscope was used at a 10 kV accelerating voltage. Samples were mounted on a carbon-taped stub and coated with platinum. EDS data were collected with Oxford Aztec software. Raman spectroscopy was performed using a Horiba LabRam HR with Duoscan imaging technology, an Olympus microscope with a 50× objective, 600 grooves/mm grating, and a Synapse CCD detector. A 532 nm laser was used with the Duoscan to yield a spot size of 5 × 5 μm. 20 spectra taken over 20 s each were averaged to generate the spectra presented in this work. TEM images were obtained using a FEI Technai G(2) F30 S-Twin 300 kV transmission electron microscope equipped with a field emission gun capable of 0.2 nm point resolution. The transmission electron microscope was operated at 300 kV under bright field, and the images were collected using a Gatan Ultrascan 1000 CCD camera. An FEI single tilt sample holder was used for all imaging experiments. EDS maps were taken with a JEOL NeoARM AC- scanning transmission electron microscope using OXFORD Aztec spectral acquisition and EDS mapping software. HEO samples were prepared for TEM by grinding in isopropanol using an agate mortar and pestle and subsequently dragging a TEM grid through the suspension to decorate the grid with HEO particles. The TEM grid was then dried under N_2. All samples were prepared using a Cu TEM grid with lacey carbon matrix. To determine elemental oxidation states, XPS spectra were measured with a Kratos AXIS DLD Ultra photoelectron spectrometer equipped with a monochromatic Al K_α source operating at 150 W. DRS measurements were taken in the UV–vis range with an Ocean Optics DT-MINI-2-GS light source and spectrometer. Reflectance spectra were smoothed through adjacent point averaging. Hydrogen temperature programmed

reduction (H_2–TPR) was conducted on select samples to evaluate high-temperature chemical resistance. Measurements were taken using a Micromeritics Autochem II 2920 using a 50 ml/min flow of 10% H_2 (balance Ar) and a heating rate of 5 °C/min up to 850 °C.

■ RESULTS AND DISCUSSION

Initial characterization results yielded compositional and structural information of spinel samples containing a single divalent cation in nominal stoichiometric ratio to aluminum. XRD patterns of these samples are shown in Figure 1a. Data are plotted as the square root of intensity to enhance the visibility of any peaks corresponding to low concentrations of secondary oxide phases. As with previous HEO studies, the cationic constituents added here demonstrate varying tendency to form secondary oxide phases dissimilar to that of the spinel structure.[1] Co_1 and Mg_1 samples calcined at 800 °C adopt phase-pure $CoAl_2O_4$ and $MgAl_2O_4$ spinel structures, respectively, while Cu_1 and Ni_1 samples contained segregated oxide phases. Cu^{2+} and Ni^{2+} ions have a higher preference for octahedral site occupancy than do Co^{2+} and Mg^{2+}.[48] Enthalpies of formation (ΔH_f) are also notably higher for $CuAl_2O_4$ and $NiAl_2O_4$ than for $CoAl_2O_4$ and $MgAl_2O_4$, which accounts for the segregation of CuO and NiO phases under initial synthesis conditions.[57] Mn_1 shows poor crystallinity, evidenced by broad peaks of low intensity. The low intensity of the Co_1 sample is likely a result of fluorescence from cobalt, which raises the background signal. Table 1 lists the EPMA compositional data, showing that the

Table 1. Physical Characterization of Stoichiometric Spinels With a Single Divalent Cation

sample	M^{2+} composition (x in M_xAl_2O4)	calcination temperature (°C)	lattice parameter (Å)[a]	average crystallite size (nm)[a]	Surface area (m^2/g)
Co_1	0.99	800	8.095	19.4	52
Cu_1	1.03	950	8.091	20.6	8
Mg_1	0.90	800	8.078	5.8	95
Mn_1	1.06	950	8.084[b]	7.4[b]	29
Ni_1	0.87	950	8.060	9.4	58

[a]Lattice parameters and average crystallite sizes listed correspond to the MAl_2O_4 phase. [b]Values are given for the predominant MAl_2O_4 phase.

actual concentrations of divalent cations were near nominal values. Since Mg showed a tendency to form a phase-pure spinel, a series of samples with varying Mg concentrations were produced to demonstrate the ability to form sub-stoichiometric compounds. The pure alumina sample synthesized without divalent metal addition has the γ-Al_2O_3 phase (Figure 1b) in which the Al^{3+} ions are known to favor octahedral sites.[45] Samples with Mg stoichiometry from 0.2 to 1 all adopted a phase-pure spinel structure. This result verifies that aluminate spinels accommodate large deviations from stoichiometry and thus large cation vacancy concentrations. These findings are corroborated by previous studies.[42,43]

In keeping with the methodology of previous HEO studies, we next evaluated the effects of increasing temperature and the number of divalent cationic species (N) on entropic stabilization of single-phase stoichiometric spinels. Cu_1, Mn_1, and Ni_1 samples previously calcined at 800 °C all showed secondary oxide phases. These samples were next calcined at 900 and 950 °C for 2 h, followed by quenching in ambient air. The

corresponding XRD patterns for Cu_1 and Ni_1 samples heated above 800 °C are shown in Figure S1. Calcination at 950 °C followed by quenching was sufficient to create phase-pure $NiAl_2O_4$ and $CuAl_2O_4$ structures, as indicated by the corresponding Rietveld refinements shown in Figure S2 and Figure S3. Raman spectra of the Ni_1—800 °C and Ni_1—950 °C samples complement these results (Figure S4). Both spectra show vibrational features corresponding to the $NiAl_2O_4$ phase.[58] However, a peak near 1100 cm^{-1} corresponding to a multi-phonon scattering mode of NiO is present in the sample calcined at 800 °C but is absent in the sample calcined at 950 °C.[59] The peaks of quenched Cu_1 are asymmetric, indicating a distribution of unit cell sizes skewed toward larger dimensions, which is likely caused by non-equilibrium mixed cation site occupation retained through rapid sample cooling. Secondary oxide phase segregation was observed when these samples were allowed to cool slowly within the furnace, as opposed to quenching. This behavior was observed in previous studies within entropically stabilized materials and is demonstrated here through XRD patterns of the Ni_1 sample shown in Figure S5. Even after aging at 950 °C, Mn_1 contained multiple phases, including two distinct $MnAl_2O_4$ phases and Mn_3O_4 (Figure S5). According to crystal field theory, Mn^{2+} ions can occupy tetrahedral and octahedral sites with no energetic preference but with different Mn–O bond lengths, which explains why two unique spinel crystal structures with distinct peak locations and lattice parameters coexist within the Mn_1 sample.[48] Lattice parameter and average crystallite size are listed for the predominant $MnAl_2O_4$ phase in Table 1. While aging at elevated temperature was effective in producing phase-pure spinels, samples were prone to sintering. Ni_1 calcined at 800 °C had a surface area of 117 m^2/g, which dropped to 52 m^2/g after heating at 950 °C. Such effects hamper the performance of spinels in surface-mediated applications, like catalysis, which incentivizes the production of spinels at lower temperatures. This effect was achieved in previous HEO studies through mixing of additional cations, which we now explore.[1]

To promote configurational entropy through cationic mixing, a set of nickel-containing spinels was synthesized with multiple divalent metals. These stoichiometric samples were all calcined at 800 °C and included Ni_1, $(MgNi)_1$, $(CoMgNi)_1$, $(CoCuMgNi)_1$, and $(CoCuMgMnNi)_1$, with the corresponding number of cationic species being N = 1 through N = 5. XRD patterns in Figure 2a,b show the diminishing presence of NiO with increasing N. Rietveld refinements (Figures S7 and S8) confirmed the presence of segregated NiO in $(CoMgNi)_1$, but the absence of this phase in $(CoCuMgNi)_1$. The pattern of $(CoCuMgMnNi)_1$ additionally showed no phases other than aluminate spinel. SEM-EDS mapping of this sample indicates a homogeneous distribution of all the constituent elements (Figure 3). EPMA analysis further confirmed that actual compositions were near target values (Table S1). The effect of calcination parameters was evaluated by comparing the structure of the $(CoCuMgNi)_1$ samples all heated to 800 °C but at varying ramp rates (5 °C/min, 25 °C/min, and with placement in a preheated furnace). All three structures were phase pure, with no significant structural differences observed via XRD patterns (Figure S9), suggesting that a phase-pure high entropy spinel is indeed thermodynamically favored at this calcination temperature. By raising entropy via increased temperature and/or number of cationic constituents, the enthalpic penalties for nickel aluminate formation were overcome, resulting in the stabilization of phase-pure spinel HEOs. Further, the sol–gel synthesis enabled compositionally homogeneous oxide for-
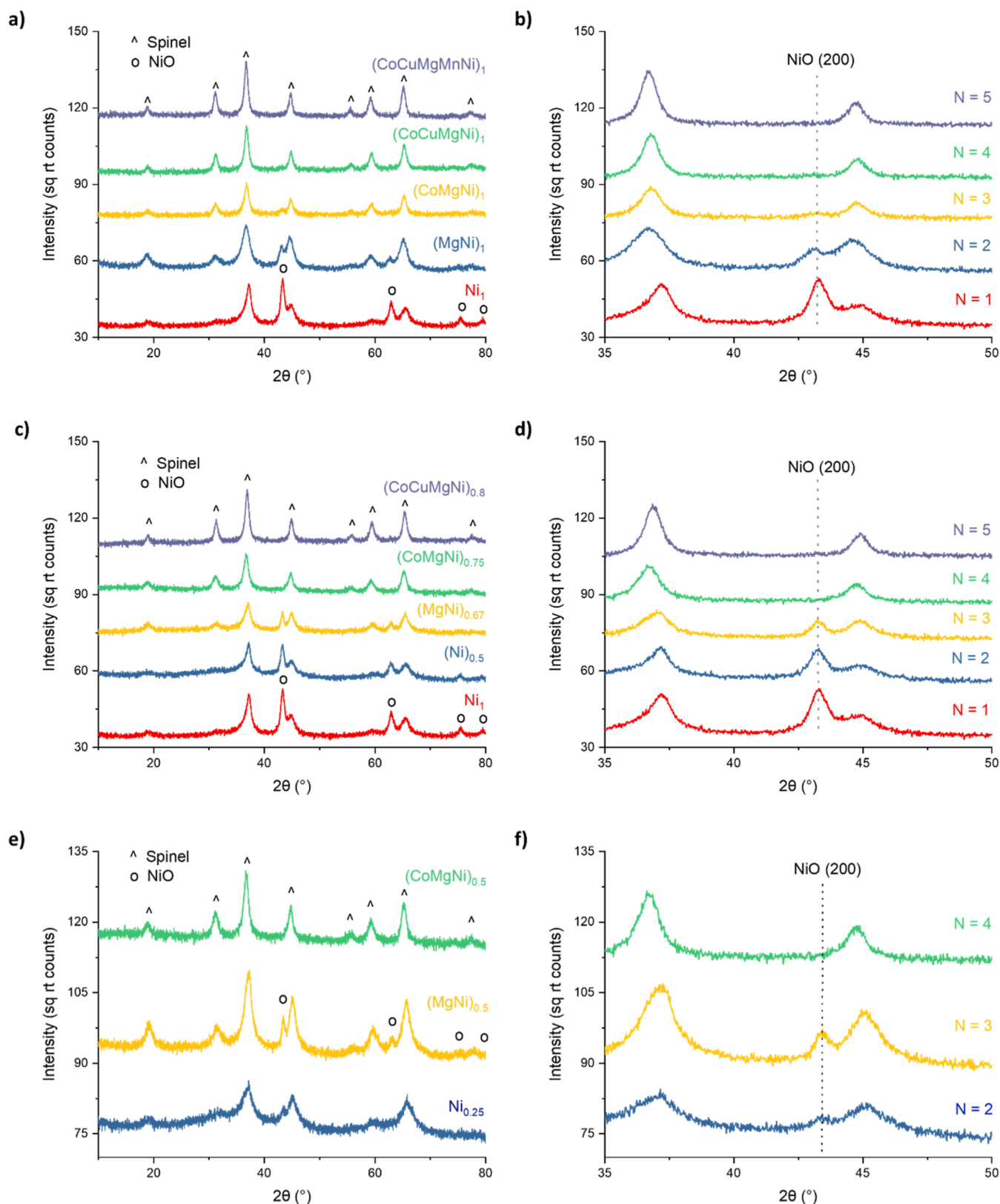
Figure 2. XRD patterns of (a,b) stoichiometric spinels and (c,d,e,f) sub-stoichiometric spinels containing varying numbers of divalent cations. All samples shown were calcined at 800 °C.

mation through aqueous precursor mixing, negating the high-temperature solid-state mixing protocols common in HEO studies.

Next, sub-stoichiometric spinels were synthesized with 800 °C calcination and characterized. Ni-containing spinels were again studied, and cationic elements were added in the same order as in the previous set of samples. However, the ratio of the
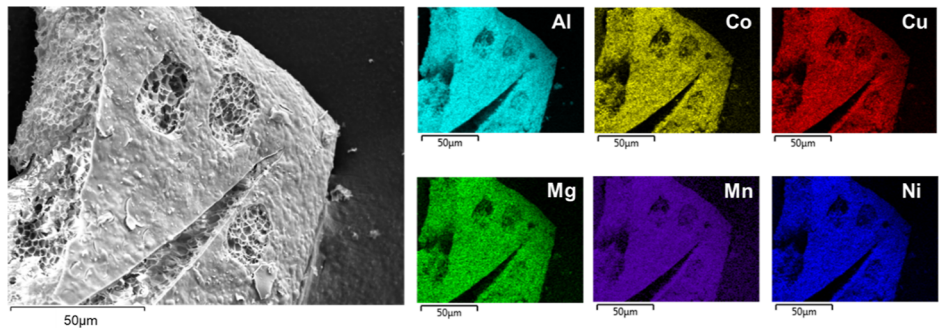
Figure 3. SEM imaging and EDS elemental mapping of the $(CoCuMgMnNi)_1$ sample showing a morphologically porous, compositionally homogeneous microstructure. Scale marker is 50 μm.

total divalent cations to Al^{3+} was <0.5, and the concentration of each divalent element was kept equimolar to the concentration of unoccupied divalent cation sites, assuming that these divalent species occupy A-sites only. The resulting samples were $Ni_{0.5}$, $(MgNi)_{0.67}$, $(CoMgNi)_{0.75}$, and $(CoCuMgNi)_{0.8}$. Compositions, lattice parameters, and average crystallite sizes of these oxides are listed in Table S2. Total divalent cation concentrations are clearly below stoichiometric values. Figure 2c,d shows the corresponding XRD patterns. As with the stoichiometric spinels, segregated NiO phase is present in spinels having up to three cationic species. The $(CoMgNi)_{0.75}$ and $(CoCuMgNi)_{0.8}$ samples having four and five cationic species, on the other hand, are phase pure. Rietveld refinements of these representative samples are shown in Figures S10 and S11. TEM imaging of the $(CoMgNi)_{0.75}$ sample confirmed a spinel structure composed of agglomerated nanoparticles, as shown in Figure 4. Interplanar distances in the lattice fringes measured with
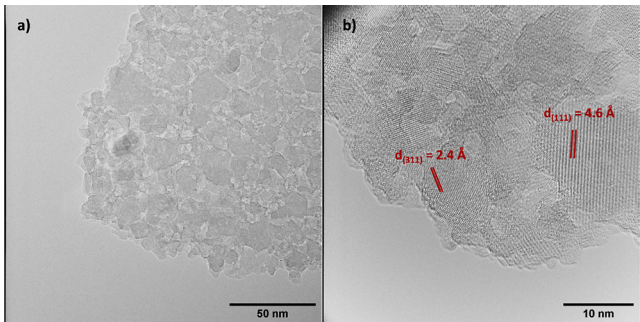

Figure 4. TEM images of the $(CoMgNi)_{0.75}$ sample showing (a) nanostructure morphology at lower magnification and (b) interplanar spacing of confirmed spinel planes at higher magnification.

ImageJ software were 4.6 and 2.4 Å, which can be indexed to the (111) and (311) planes, respectively, of the nickel and magnesium aluminate spinels. TEM-EDS mapping further shows uniform elemental distribution throughout the sample,

with no phase segregation evident (Figure S12). The stoichiometries of Co, Mg, and Ni with the $(CoMgNi)_{0.75}$ sample are 0.24, 0.32, and 0.22, respectively, as measured via averaged EDS spectra. These values are in excellent agreement with EPMA measurements.

In HEO spinels, divalent cations compete for limited available lattice sites, and varying diffusion rates could limit the integration of kinetically slower species, leading to segregated oxide phases. To rule out the competing effects of other divalent cations, we evaluated the $Ni_{0.25}$ and $(MgNi)_{0.5}$ samples via XRD, which had lower Mg concentrations and higher vacancy concentrations than those previously shown in an effort to increase the Ni diffusion rates.[60] Despite these factors, NiO segregation was evident in both the $Ni_{0.25}$ and $(MgNi)_{0.5}$ samples, suggesting that Ni ions are not kinetically hindered from incorporating into the spinel lattice under our synthesis conditions. Detection of the NiO phase within the $Ni_{0.25}$ sample further excludes decreased nickel content as an explanation for the absence of detectable NiO peaks in the XRD patterns of phase-pure $(CoMgNi)_{0.75}$ and $(CoCuMgNi)_1$. However, segregation of NiO (even at low Ni loadings) is rational in the context of entropic stabilization, in that a lower number of cationic species and deviation from equimolar cation concentrations does not provide enough entropy to overcome the relatively high enthalpic terms associated with nickel aluminate phase formation.[57] The persistent finding that four cationic species are required to stabilize phase-pure Ni-containing spinels at the same temperature is consistent with the principles of entropic stabilization. Since this behavior is consistent between stoichiometric and sub-stoichiometric spinels, we conclude that cationic vacancies contribute to configurational entropy similarly to cations and can stabilize phase-pure HEOs.

The structural features of select samples were further evaluated to estimate cationic and anionic site occupation. Measured XRD patterns were fit via Rietveld refinement and compared to simulated patterns with varying cation compositions and site occupancies, as demonstrated in previous literature.[47,61] Because diffraction peak intensity is a function

Table 2. Measured Compositions and Site Occupancies Modeled Through Rietveld Refinement of Select Spinel Samples

sample	measured total M^{2+} composition (x in $MxAl2Oz$)	lattice parameter (Å)	A-site occupancy	B-site occupancy	O-site occupancy
Mg_1	0.90	8.078	Mg_1	Al_2	O_4
Ni_1	0.99	8.056	Al_1	Al_1Ni_1	O_4
$Ni_{0.75}$	0.76	8.047	$Al_{0.98}$	$Al_{1.02}Ni_{0.76}$	$O_{3.82}$
$Ni_{0.5}$	0.49	8.032	$Al_{0.9}$	$Al_{1.1}Ni_{0.56}$	$O_{3.56}$
$(CoCuMgNi)_1$	1.01	8.077	$Al_{0.2}M_{0.69}$	$Al_{1.8}M_{0.22}$	$O_{3.35}$
$(CoMgNi)_{0.75}$	0.81	8.069	$Al_{0.1}M_{0.52}$	$Al_{1.9}M_{0.1}$	$O_{3.6}$

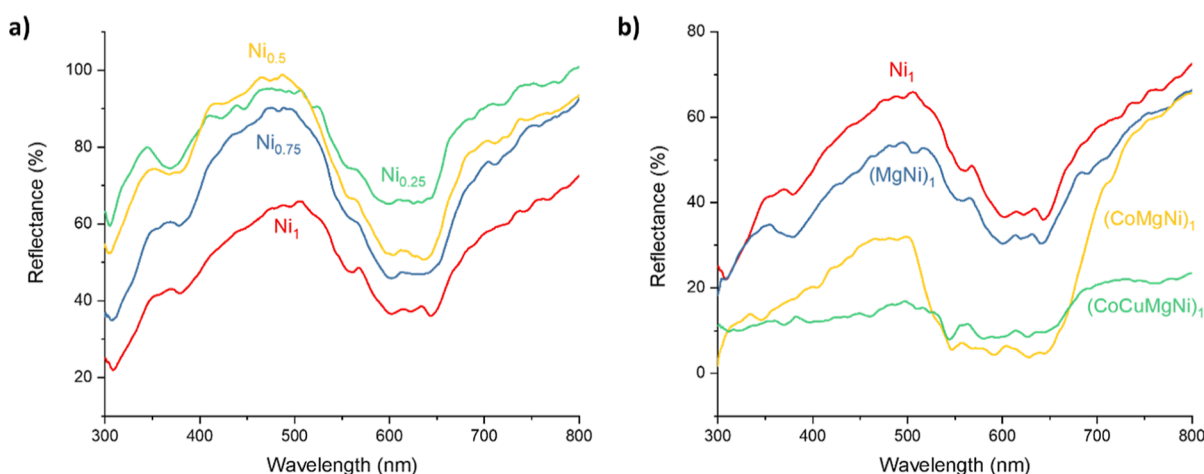**Figure 5.** Reflectance spectra of nickel aluminate spinels with (a) varying $Ni^{2+}:Al^{3+}$ ratio and (b) addition of other divalent cations.

of the size and electron density of atoms within a given crystallographic plane, the relative peak intensities can be used to determine the distribution of cations occupying A and B sites. As exemplified by nickel aluminates (Figure S13), simulated patterns show variation in relative peak intensity, most notably between (111) and (220) peaks, when changing the relative site occupation of Ni^{2+} and Al^{3+} cations. Measured patterns of the Mg_1 and Ni_1 samples were first evaluated, which are known to adopt normal and inverse spinel structures, respectively. As expected, Rietveld refinement indicates that all Mg^{2+} ions occupy tetrahedral A-sites and all Ni^{2+} ions occupy octahedral B-sites, while oxygen sites in these stoichiometric structures are completely filled (Table 2). This finding corroborates the entropic stabilization of $NiAl_2O_4$ observed in our heat treatment studies, as well as in prior literature.[46] The presence of both Al^{3+} and Ni^{2+} ions in B-sites creates non-negligible configuration entropy. Ni^{2+} ions occupy B-sites exclusively in the non-stoichiometric $Ni_{0.75}$ and $Ni_{0.5}$ samples as well. Refinements of these patterns also indicate the presence of cationic and anionic vacancies. The total occupation of cationic and anionic sites decreases in spinels with low Ni^{2+}/Al^{3+} ratios and indicates that the non-stoichiometric structures are highly defected. A decrease in spinel lattice parameter is also consistent with higher vacancy concentrations.[41,42]

While a direct determination of oxygen stoichiometry via Rietveld refinement is unreliable, anion site occupation was calculated based on measured elemental compositions, cation site occupation, and elemental oxidation states (measured via XPS, as shown in Figure S14), assuming charge neutrality of the oxide samples. XPS spectra taken of the transition metals within $(CoCuMgNi)_{0.8}$ show that Co, Cu, and Ni exist as divalent species. Because the oxidation state of these metals in the starting precursors was the same as that in the prepared oxides, we conclude that redox reactions did not play a charge-compensating role in the formation of sub-stoichiometric spinels. As such, oxygen vacancy formation is reasonably assumed to be the charge compensating mechanism for variations in the cation concentration. As predicted, refinements of the stoichiometric Ni_1 and Mg_1 samples found the oxygen sub-lattice to be fully occupied. However, initial refinements of sub-stoichiometric nickel and HEO spinels resisted progression toward solution when the anionic sub-lattice was assumed to be fully occupied. This issue was overcome by enabling oxygen vacancies in the refinement. Resulting refinements of the $Ni_{0.75}$

and $Ni_{0.5}$ samples indicate increasing oxygen vacancy concentration with nickel sub-stoichiometry, which agrees with composition and oxidation state measurements, as well as charge neutrality assumptions.

Spinels containing multiple divalent cations are more difficult to model. For simplification, these species were treated as a single element with electron density that was the average of all divalent cationic species, as validated by XPS data. As shown in Table 2, Al^{3+} and M^{2+} cations occupy both tetrahedral and octahedral sites within the $(CoCuMgNi)_1$ and $(CoMgNi)_{0.75}$ samples. However, the degree of inversion is lower in these HEO spinels, with a majority of the M^{2+} ions occupying tetrahedral sites. This is expected with the addition of Mg^{2+} and Co^{2+} ions, which have much higher energetic preference for tetrahedral site occupation than Ni^{2+}.[48] Inclusion of both divalent cations that prefer normal and inverse spinel structures creates mixed occupations on both A and B lattice sites. The complex structures that result from multiple cationic constituent inclusion and with non-stoichiometric ratios enable all three sub-lattices of aluminate spinels to contribute to configurational entropy, which is inherently unachievable in many HEO material systems.

We next evaluated the role of stoichiometry and compositional complexity on material properties relevant to applied aluminate spinels. $NiAl_2O_4$, $CoAl_2O_4$, and $CuAl_2O_4$ spinels commonly serve as cyan, blue, and red-brown pigments in paints, dyes, inks, and other aesthetic coatings.[62−64] The color of these metal oxides is known to be influenced by structural parameters relevant to the synthesis method used and transition metal constituents.[64] Figure 5a shows the spectra of nickel spinels with varying Ni/Al ratios, all calcined at 950 °C and quenched. The spectra of Ni_1 is comparable to that reported previously for nickel aluminate spinels, with absorption bands near 380 and from 600 to 645 nm ascribed to $v_3[^3A_{2g} \rightarrow {}^3T_{1g}(P)]$ and $[^3T_1(F) \rightarrow {}^3T_{1g}(P)]$ electronic transitions of Ni^{2+} within the spinel structure.[43] Lowering the Ni:Al ratio below stoichiometric values increases reflectivity across the visible spectrum, in agreement with previous observations.[42] CIELAB color space measurements were taken to quantify changes in lightness and coloration (Table S3). Lightness, measured as L*, consistently decreased with increasing content of photo-absorbing nickel cations. $a*$ and $b*$ values were primarily negative for this sample set, indicating green-blue coloration characteristic of nickel aluminates.[62] Digital images of these

samples and others are given in Figure S15, which show significant variation in color achieved by modulating the M^{2+}/Al^{3+} stoichiometry in nickel, copper, and cobalt aluminates. Non-stoichiometric spinels clearly adopt unique colors un-achieved in the stoichiometric oxide and provide a wider range of pigment properties.

The incorporation of multiple divalent cationic elements was next evaluated with spectra shown in Figure 5b. Spectral features are similar for the Ni_1 and $(MgNi)_1$ samples, since magnesium does not significantly absorb visible light. Co-addition of cobalt lowers reflectance across the visible spectrum, particularly in the 500−700 nm range. This absorption band is ascribed to the $^4A_2(F) \rightarrow {}^4T_1(P)$ transition of the Co^{2+} ions within an aluminate spinel structure.[63,65] Reflectance of $(CoCuMgNi)_1$ is lowered substantially through the addition of copper, which exhibits broad absorption bands across the visible spectrum due to charge transfer between oxygen anions and Cu^{2+} occupying octahedral sites.[64] As shown, HEO spinels can be highly effective UV−vis absorbers via incorporation of multiple transition metal constituents, which absorb light over different wavelength ranges. Tunable light absorption properties, along with the excellent thermal stability of aluminate spinels, give these materials great potential for photocatalytic and solar thermal applications.[66,67]

Aluminate spinels are commonly used in high-temperature environments due to their excellent thermal stability. However, the desired chemical properties of these spinels are application dependent. Chemical inertness is required of refractory spinel materials,[54] while spinel catalysts must exhibit chemical interaction with reactant molecules and even be structurally reducible to form catalytically active metallic phases.[42] To assess the effect of vacancies and multiple divalent metals on spinel stability, select Ni-containing samples were evaluated through hydrogen temperature programmed reduction (H_2−TPR). Each of these samples was calcined at sufficiently high temperatures and quenched to form a phase-pure spinel prior to analysis. Figure 6 shows the resulting profiles with the temperature of the reduction peaks labeled. All primary reduction peaks occur at temperatures well over 700 °C and correspond to reduction of the nickel aluminate phase.[68] The reduction mechanism was previously identified as a separation of

nickel from the spinel lattice to form metallic nickel and alumina phases.[69] Of the spinels evaluated, Ni_1 shows the lowest reduction peak temperature at 770 °C, at which point the spinel structure is compromised. Inclusion of Co and Mg shifts the reduction peak to higher temperatures. This result agrees with previous observations that $CoAl_2O_4$ and $MgAl_2O_4$ spinels are less reducible than $NiAl_2O_4$.[70] The reduction peak is also shifted to higher temperatures through vacancy inclusion. This shift was as large as 51 °C between the Ni_1 and $Ni_{0.5}$ samples, suggesting that sub-stoichiometric spinels withstand chemically aggressive environments at higher temperatures compared to their stoichiometric counterparts. While alumina achieves excellent chemical resistance without divalent metal constituents, alumina phase changes occurring above 800 °C significantly alter the material structure.[71] Spinel phases, on the other hand, are thermally stable at higher temperatures, but are more chemically reactive in the conventional stoichiometric form. Since sub-stoichiometric spinels showed no alumina phases, even after 950 °C aging, and showed increased reduction peak temperatures, we find that cationic vacancies provide a valuable parameter for optimizing desired thermal and chemical properties, which are unachieved in alumina and conventional stoichiometric spinels. Cationic vacancies yield the added benefit of reducing processing temperatures (and therefore energy), as well as the use of transition metals, many of which are rare yet critical elements needed for emerging technologies.

CONCLUSIONS

In this work, we present complex aluminate spinels stabilized with cation vacancies as a new high entropy oxide material system. The unique ability of aluminate spinels to accommodate large deviations below stoichiometry enables a systematic study of vacancy-contributed configurational entropy. Presence of both cationic and anionic vacancies, as well as cation inversion, was confirmed in HEO samples. These structural features increased configurational entropy and aided the stabilization of phase-pure complex spinel oxides. Entropy effects, as well as our use of a sol−gel synthesis, significantly lowered the processing temperature required to form phase-pure spinels compared to solid-state reactions. Incorporation of high cation vacancy concentrations and multiple divalent metals yields highly tunable structural, chromatic, and chemical properties. These properties enhance the potential of high entropy and sub-stoichiometric spinels as unique pigments, photo absorbents, refractories, and catalysts. In sum, we propose that the concept of vacancy-stabilized high entropy oxides be applied intention-ally to other non-stoichiometric complex oxides with crystal structures having multiple cationic lattice sites, including other spinel, perovskite, and pyrochlore material systems.

ASSOCIATED CONTENT

Supporting Information

The Supporting Information is available free of charge at https://pubs.acs.org/doi/10.1021/acs.jpcc.3c01499.

XRD patterns, Rietveld refinements, EPMA compositions, Raman spectra, and digital images of prepared samples (PDF)

Figure 6. H_2−TPR profiles of select phase-pure Ni-containing spinel samples.

AUTHOR INFORMATION

Corresponding Author

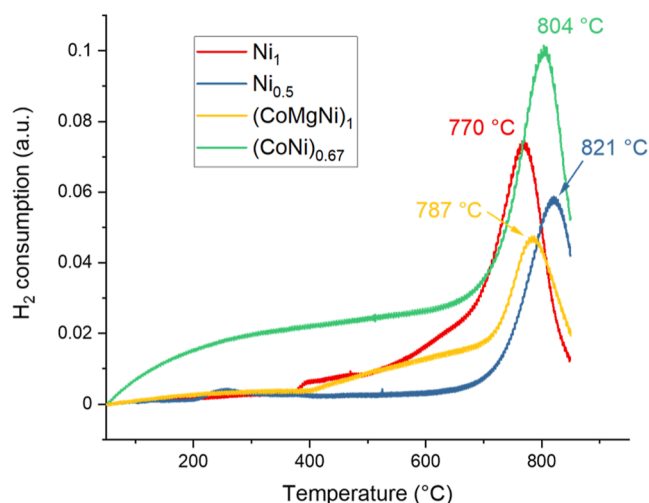**Christopher Riley** − *Sandia National Laboratories, Albuquerque, New Mexico 87185, United States;*

orcid.org/0000-0002-6403-0677; Email: crriley@sandia.gov

Authors

Nichole Valdez − *Sandia National Laboratories, Albuquerque, New Mexico 87185, United States*

Christopher M. Smyth − *Sandia National Laboratories, Albuquerque, New Mexico 87185, United States;* orcid.org/0000-0003-4668-9555

Richard Grant − *Sandia National Laboratories, Albuquerque, New Mexico 87185, United States*

Brandon Burnside − *Department of Chemical and Biological Engineering and Center for Microengineered Materials, University of New Mexico, Albuquerque, New Mexico 87131, United States*

James Eujin Park − *Sandia National Laboratories, Albuquerque, New Mexico 87185, United States;* orcid.org/0000-0003-2128-9811

Stephen Meserole − *Sandia National Laboratories, Albuquerque, New Mexico 87185, United States*

Angelica Benavidez − *Department of Chemical and Biological Engineering and Center for Microengineered Materials, University of New Mexico, Albuquerque, New Mexico 87131, United States*

Robert Craig − *Sandia National Laboratories, Albuquerque, New Mexico 87185, United States*

Stephen Porter − *Department of Chemical and Biological Engineering and Center for Microengineered Materials, University of New Mexico, Albuquerque, New Mexico 87131, United States;* orcid.org/0000-0002-4529-4036

Andrew DeLaRiva − *Department of Chemical and Biological Engineering and Center for Microengineered Materials, University of New Mexico, Albuquerque, New Mexico 87131, United States*

Abhaya Datye − *Department of Chemical and Biological Engineering and Center for Microengineered Materials, University of New Mexico, Albuquerque, New Mexico 87131, United States;* orcid.org/0000-0002-7126-8659

Mark Rodriguez − *Sandia National Laboratories, Albuquerque, New Mexico 87185, United States*

Stanley S. Chou − *Sandia National Laboratories, Albuquerque, New Mexico 87185, United States;* orcid.org/0000-0003-3655-6185

Complete contact information is available at:
https://pubs.acs.org/10.1021/acs.jpcc.3c01499

Notes

The authors declare no competing financial interest.

REFERENCES

(1) Rost, C. M.; Sachet, E.; Borman, T.; Moballegh, A.; Dickey, E. C.; Hou, D.; Jones, J. L.; Curtarolo, S.; Maria, J. P. Entropy-Stabilized Oxides. *Nat. Commun.* **2015**, *6*, 8485.

(2) Sarkar, A.; Velasco, L.; Wang, D.; Wang, Q.; Talasila, G.; de Biasi, L.; Kübel, C.; Brezesinski, T.; Bhattacharya, S. S.; Hahn, H.; et al. High Entropy Oxides for Reversible Energy Storage. *Nat. Commun.* **2018**, *9*, 3400.

(3) Gild, J.; Samiee, M.; Braun, J. L.; Harrington, T.; Vega, H.; Hopkins, P. E.; Vecchio, K.; Luo, J. High-Entropy Fluorite Oxides. *J. Eur. Ceram. Soc.* **2018**, *38*, 3578−3584.

(4) Chellali, M. R.; Sarkar, A.; Nandam, S. H.; Bhattacharya, S. S.; Breitung, B.; Hahn, H.; Velasco, L. On the Homogeneity of High Entropy Oxides: An Investigation at the Atomic Scale. *Scr. Mater.* **2019**, *166*, 58−63.

(5) Shu, Y.; Bao, J.; Yang, S.; Duan, X.; Zhang, P. Entropy Stabilized Metal Ceo$_x$ Solid Solutions for Catalytic Combustion of Volatile Organic Compounds. *AIChE J.* **2020**, *67*, DOI: 10.1002/aic.17046.

(6) Grzesik, Z.; Smoła, G.; Miszczak, M.; Stygar, M.; Dąbrowa, J.; Zajusz, M.; Świerczek, K.; Danielewski, M. Defect Structure and Transport Properties of (Co,Cr,Fe,Mn,Ni)$_3$O$_4$ Spinel-Structured High Entropy Oxide. *J. Eur. Ceram. Soc.* **2020**, *40*, 835−839.

(7) Wang, D.; Liu, Z.; Du, S.; Zhang, Y.; Li, H.; Xiao, Z.; Chen, W.; Chen, R.; Wang, Y.; Zou, Y.; et al. Low-Temperature Synthesis of Small-Sized High-Entropy Oxides for Water Oxidation. *J. Mater. Chem. A* **2019**, *7*, 24211−24216.

(8) Zhang, Y.; Lu, T.; Ye, Y.; Dai, W.; Zhu, Y.; Pan, Y. Stabilizing Oxygen Vacancy in Entropy-Engineered CoFe$_2$O$_4$-Type Catalysts for Co-Prosperity of Efficiency and Stability in an Oxygen Evolution Reaction. *ACS Appl. Mater. Interfaces* **2020**, *12*, 32548−32555.

(9) Banerjee, R.; Chatterjee, S.; Ranjan, M.; Bhattacharya, T.; Mukherjee, S.; Jana, S. S.; Dwivedi, A.; Maiti, T. High-Entropy Perovskites: An Emergent Class of Oxide Thermoelectrics with Ultralow Thermal Conductivity. *ACS Sustainable Chem. Eng.* **2020**, *8*, 17022−17032.

(10) Sarkar, A.; Djenadic, R.; Wang, D.; Hein, C.; Kautenburger, R.; Clemens, O.; Hahn, H. Rare Earth and Transition Metal Based Entropy Stabilised Perovskite Type Oxides. *J. Eur. Ceram. Soc.* **2018**, *38*, 2318−2327.

(11) Hou, S.; Ma, X.; Shu, Y.; Bao, J.; Zhang, Q.; Chen, M.; Zhang, P.; Dai, S. Self-Regeneration of Supported Transition Metals by a High Entropy-Driven Principle. *Nat. Commun.* **2021**, *12*, 5917.

(12) Bérardan, D.; Franger, S.; Meena, A. K.; Dragoe, N. Room Temperature Lithium Superionic Conductivity in High Entropy Oxides. *J. Mater. Chem. A* **2016**, *4*, 9536−9541.

(13) Bérardan, D.; Franger, S.; Dragoe, D.; Meena, A. K.; Dragoe, N. Colossal Dielectric Constant in High Entropy Oxides. *Phys. Status Solidi Rapid Res. Lett.* **2016**, *10*, 328−333.

(14) Chen, H.; Fu, J.; Zhang, P.; Peng, H.; Abney, C. W.; Jie, K.; Liu, X.; Chi, M.; Dai, S. Entropy-Stabilized Metal Oxide Solid Solutions as Co Oxidation Catalysts with High-Temperature Stability. *J. Mater. Chem. A* **2018**, *6*, 11129−11133.

(15) Riley, C.; De La Riva, A.; Park, J. E.; Percival, S. J.; Benavidez, A.; Coker, E. N.; Aidun, R. E.; Paisley, E. A.; Datye, A.; Chou, S. S. A High Entropy Oxide Designed to Catalyze Co Oxidation without Precious Metals. *ACS Appl. Mater. Interfaces* **2021**, *13*, 8120−8128.

(16) Zhao, J.; Bao, J.; Yang, S.; Niu, Q.; Xie, R.; Zhang, Q.; Chen, M.; Zhang, P.; Dai, S. Exsolution−Dissolution of Supported Metals on High-Entropy Co3mnnicuznox: Toward Sintering-Resistant Catalysis. *ACS Catal.* **2021**, *11*, 12247−12257.

(17) Dąbrowa, J.; Stygar, M.; Mikuła, A.; Knapik, A.; Mroczka, K.; Tejchman, W.; Danielewski, M.; Martin, M. Synthesis and Micro-

structure of the $(Co,Cr,Fe,Mn,Ni)_3O_4$ High Entropy Oxide Characterized by Spinel Structure. *Mater. Lett.* **2018**, *216*, 32−36.

(18) Dabrowa, J.; Zielinska, K.; Stepien, A.; Zajusz, M.; Nowakowska, M.; Mozdzierz, M.; Berent, K.; Szymczak, M.; Swierczek, K. Formation of Solid Solutions and Physicochemical Properties of the High-Entropy $Ln_{(1-X)}Sr_{(X)}(Co,Cr,Fe,Mn,Ni)O_{(3-\Delta)}$ (Ln = La, Pr, Nd, Sm or Gd) Perovskites. *Materials* **2021**, *14*, 5264.

(19) Dippo, O. F.; Vecchio, K. S. A Universal Configurational Entropy Metric for High-Entropy Materials. *Scr. Mater.* **2021**, *201*, 113974.

(20) Sarkar, A.; Breitung, B.; Hahn, H. High Entropy Oxides: The Role of Entropy, Enthalpy and Synergy. *Scr. Mater.* **2020**, *187*, 43−48.

(21) Bulfin, B.; Hoffmann, L.; de Oliveira, L.; Knoblauch, N.; Call, F.; Roeb, M.; Sattler, C.; Schmucker, M. Statistical Thermodynamics of Non-Stoichiometric Ceria and Ceria Zirconia Solid Solutions. *Phys. Chem. Chem. Phys.* **2016**, *18*, 23147−23154.

(22) Djenadic, R.; Sarkar, A.; Clemens, O.; Loho, C.; Botros, M.; Chakravadhanula, V. S. K.; Kübel, C.; Bhattacharya, S. S.; Gandhi, A. S.; Hahn, H. Multicomponent Equiatomic Rare Earth Oxides. *Mater. Res. Lett.* **2016**, *5*, 102−109.

(23) Yuan, F.; Zhang, Y.; Weber, W. J. Vacancy−Vacancy Interaction Induced Oxygen Diffusivity Enhancement in Undoped Nonstoichiometric Ceria. *J. Phys. Chem. C* **2015**, *119*, 13153−13159.

(24) Ferrari, A. M.; Pisani, C.; Cinquini, F.; Giordano, L.; Pacchioni, G. Cationic and Anionic Vacancies on the Nio(100) Surface: Dft+U and Hybrid Functional Density Functional Theory Calculations. *J. Chem. Phys.* **2007**, *127*, 174711.

(25) Moździerz, M.; Dąbrowa, J.; Stępień, A.; Zajusz, M.; Stygar, M.; Zając, W.; Danielewski, M.; Świerczek, K. Mixed Ionic-Electronic Transport in the High-Entropy $(Co,Cu,Mg,Ni,Zn)_1$-LiO Oxides. *Acta Mater.* **2021**, *208*, 116735.

(26) Liu, X.; Xing, Y.; Xu, K.; Zhang, H.; Gong, M.; Jia, Q.; Zhang, S.; Lei, W. Kinetically Accelerated Lithium Storage in High-Entropy (LiMgCoNiCuZn)O Enabled by Oxygen Vacancies. *Small* **2022**, *18*, No. e2200524.

(27) Ting, C.-J.; Lu, H.-Y. Defect Reactions and the Controlling Mechanism in the Sintering of Magnesium Aluminate Spinel. *J. Am. Ceram. Soc.* **1999**, *82*, 841−848.

(28) Osenciat, N.; Bérardan, D.; Dragoe, D.; Léridon, B.; Holé, S.; Meena, A. K.; Franger, S.; Dragoe, N. Charge Compensation Mechanisms in Li Substituted High Entropy Oxides and Influence on Li Superionic Conductivity. *J. Am. Ceram. Soc.* **2019**, *102*, 6156−6162.

(29) Castle, E.; Csanadi, T.; Grasso, S.; Dusza, J.; Reece, M. Processing and Properties of High-Entropy Ultra-High Temperature Carbides. *Sci. Rep.* **2018**, *8*, 8609.

(30) Sarker, P.; Harrington, T.; Toher, C.; Oses, C.; Samiee, M.; Maria, J. P.; Brenner, D. W.; Vecchio, K. S.; Curtarolo, S. High-Entropy High-Hardness Metal Carbides Discovered by Entropy Descriptors. *Nat. Commun.* **2018**, *9*, 4980.

(31) Gild, J.; Braun, J.; Kaufmann, K.; Marin, E.; Harrington, T.; Hopkins, P.; Vecchio, K.; Luo, J. A High-Entropy Silicide: $(Mo_{0.2}Nb_{0.2}Ta_{0.2}Ti_{0.2}W_{0.2})Si_2$. *J Materiomics* **2019**, *5*, 337−343.

(32) Qin, Y.; Liu, J.-X.; Li, F.; Wei, X.; Wu, H.; Zhang, G. J. A High Entropy Silicide by Reactive Spark Plasma Sintering. *J. Adv. Ceram.* **2019**, *8*, 148−152.

(33) Gild, J.; Zhang, Y.; Harrington, T.; Jiang, S.; Hu, T.; Quinn, M. C.; Mellor, W. M.; Zhou, N.; Vecchio, K.; Luo, J. High-Entropy Metal Diborides: A New Class of High-Entropy Materials and a New Type of Ultrahigh Temperature Ceramics. *Sci. Rep.* **2016**, *6*, 37946.

(34) Zhang, Y.; Jiang, Z.-B.; Sun, S.-K.; Guo, W.-M.; Chen, Q.-S.; Qiu, J.-X.; Plucknett, K.; Lin, H.-T. Microstructure and Mechanical Properties of High-Entropy Borides Derived from Boro/Carbothermal Reduction. *J. Eur. Ceram. Soc.* **2019**, *39*, 3920−3924.

(35) Zhang, Y.; Guo, W.-M.; Jiang, Z.-B.; Zhu, Q.-Q.; Sun, S.-K.; You, Y.; Plucknett, K.; Lin, H.-T. Dense High-Entropy Boride Ceramics with Ultra-High Hardness. *Scr. Mater.* **2019**, *164*, 135−139.

(36) Zhang, R. Z.; Gucci, F.; Zhu, H.; Chen, K.; Reece, M. J. Data-Driven Design of Ecofriendly Thermoelectric High-Entropy Sulfides. *Inorg. Chem.* **2018**, *57*, 13027−13033.

(37) McCormick, C. R.; Schaak, R. E. Simultaneous Multication Exchange Pathway to High-Entropy Metal Sulfide Nanoparticles. *J. Am. Chem. Soc.* **2021**, *143*, 1017−1023.

(38) Cui, M.; Yang, C.; Li, B.; Dong, Q.; Wu, M.; Hwang, S.; Xie, H.; Wang, X.; Wang, G.; Hu, L. High Entropy Metal Sulfide Nanoparticles Promise High Performance Oxygen Evolution Reaction. *Adv. Energy Mater.* **2020**, *11*, 2002887.

(39) Peng, C.; Tang, H.; He, Y.; Lu, X.; Jia, P.; Liu, G.; Zhao, Y.; Wang, M. A Novel Non-Stoichiometric Medium-Entropy Carbide Stabilized by Anion Vacancies. *J Mater Sci Technol* **2020**, *51*, 161−166.

(40) He, Y.; Peng, C.; Xin, S.; Li, K.; Liang, S.; Lu, X.; Kang, N.; Xue, H.; Shen, X.; Shen, T.; et al. Vacancy Effect on the Preparation of High-Entropy Carbides. *J. Mater. Sci.* **2020**, *55*, 6754−6760.

(41) Li, Y.; Yang, D.; Liu, C.; Yang, P.; Mu, P.; Wen, J.; Chen, S.; Li, Y. Preparation and Characterization of Novel Nonstoichiometric Magnesium Aluminate Spinels. *Ceram. Int.* **2018**, *44*, 15104−15109.

(42) Zhang, S.; Ying, M.; Yu, J.; Zhan, W.; Wang, L.; Guo, Y.; Guo, Y. $Ni_xAl_1O_{2-\Delta}$ Mesoporous Catalysts for Dry Reforming of Methane: The Special Role of $Nial_2O_4$ Spinel Phase and Its Reaction Mechanism. *Appl. Catal. B* **2021**, *291*, 120074.

(43) Gil-Calvo, M.; Jiménez-González, C.; de Rivas, B.; Gutiérrez-Ortiz, J. I.; López-Fonseca, R. Effect of Ni/Al Molar Ratio on the Performance of Substoichiometric $NiAl_2O_4$ Spinel-Based Catalysts for Partial Oxidation of Methane. *Appl. Catal. B* **2017**, *209*, 128−138.

(44) Prins, R. On the Structure of Γ-Al_2O_3. *J. Catal.* **2020**, *392*, 336−346.

(45) Lee, M.; Cheng, C.-F.; Heine, V.; Klinowski, J. Distribution of tetrahedral and octahedral A1 sites in gamma alumina. *Chem. Phys. Lett.* **1997**, *265*, 673−676.

(46) O'Neill, H. S. t. C.; Dollase, W. A.; Ross, C. R. I. Temperature Dependence of the Cation Distribution in Nickel Aluminate ($NiAl_2O_4$) Spinel: A Powder Xrd Study. *Phys Chem Minerals* **1991**, *18*, 302−319.

(47) Yan, J.; Huang, J.; Zhang, T.; Tian, H.; Yu, J.; Zhang, L.; Zhang, Y. Investigation of the Microstructure, Cation Distribution and Optical Properties of Nanoscale $Ni_xMg_{1-X}Al_2O_4$ Spinel Pigments. *Ceram. Int.* **2019**, *45*, 14073−14083.

(48) McClure, D. The Distribution of Transition Metal Cations in Spinels. *J. Phys. Chem. Solids* **1957**, *3*, 311−317.

(49) Lavina, B.; Salviulo, G.; Giusta, A. D. Cation Distribution and Structure Modelling of Spinel Solid Solutions. *Phys. Chem. Miner.* **2002**, *29*, 10−18.

(50) O'Neill, H. S. t. C.; James, M.; Dollase, W. A.; Redfern, S. A. T. Temperature Dependence of the Cation Distribution in $CuAl_2O4$ Spinel. *Eur. J. Mineral.* **2005**, *17*, 581−586.

(51) Cooley, R. F.; Reed, J. S. Equilibrium Cation Distribution in $NiAl_2O_4$, $CuAl_2O_4$, and $ZnAl_2O_4$ Spinels. *J. Am. Ceram. Soc.* **1972**, *55*, 395−398.

(52) Gaudon, M.; Robertson, L. C.; Lataste, E.; Duttine, M.; Ménétrier, M.; Demourgues, A. Cobalt and Nickel Aluminate Spinels: Blue and Cyan Pigments. *Ceram. Int.* **2014**, *40*, 5201−5207.

(53) Buvaneswari, G.; Aswathy, V.; Rajakumari, R. Comparison of Color and Optical Absorbance Properties of Divalent Ion Substituted Cu and Zn Aluminate Spinel Oxides Synthesized by Combustion Method Towards Pigment Application. *Dyes Pigm.* **2015**, *123*, 413−419.

(54) Tang, H.; Li, C.; Gao, J.; Touzo, B.; Liu, C.; Yuan, W. Optimization of Properties for Alumina-Spinel Refractory Castables by Cma (CaO-MgO-Al_2O_3) Aggregates. *Materials* **2021**, *14*, 3050.

(55) Riley, C.; De La Riva, A.; Zhou, S.; Wan, Q.; Peterson, E.; Artyushkova, K.; Farahani, M. D.; Friedrich, H. B.; Burkemper, L.; Atudorei, N.; et al. Synthesis of Nickel Doped Ceria Catalysts for Selective Acetylene Hydrogenation. *ChemCatChem* **2019**, *11*, 1526−1533.

(56) Riley, C.; Canning, G.; De La Riva, A.; Zhou, S.; Peterson, E.; Boubnov, A.; Hoffman, A.; Tran, M.; Bare, S. R.; Lin, S.; et al. Environmentally Benign Synthesis of a PGM-Free Catalyst for Low Temperature CO Oxidation. *Appl. Catal. B* **2020**, *264*, 118547.

(57) Navrotsky, A.; Kleppa, O. Thermodynamics of Formation of Simple Spinels. *J. inorg. nucl. chem.* **1968**, *30*, 479−498.

(58) Gao, Y.; Wang, S.; Lv, L.; Li, D.; Yue, X.; Wang, S. Insights into the Behaviors of the Catalytic Combustion of Propane over Spinel Catalysts. *Catal. Lett.* **2020**, *150*, 3617−3625.

(59) Mironova-Ulmane, N.; Kuzmin, A.; Steins, I.; Grabis, J.; Sildos, I.; Pärs, M. Raman Scattering in Nanosized Nickel Oxide NiO. *J. Phys. Conf. Ser* **2007**, *93*, 012039.

(60) yamaguchi, G.; Nakano, M.; Tosaki, M. Effects of Cation Vacancies of the Diffusion of Nickel Ions in Defective Spinels. *Chem. Soc. Jpn.* **1969**, *42*, 2801−2807.

(61) Tangcharoen, T.; Klysubun, W.; Kongmark, C. Synchrotron X-Ray Absorption Spectroscopy and Cation Distribution Studies of $NiAl_2O_4$, $CuAl_2O_4$, and $ZnAl_2O_4$ Nanoparticles Synthesized by Sol-Gel Auto Combustion Method. *J. Mol. Struct.* **2019**, *1182*, 219−229.

(62) Serment, B.; Gaudon, M.; Demourgues, A.; Noel, A.; Fleury, G.; Cloutet, E.; Hadziioannou, G.; Brochon, C. Cyan $Ni_{1-x}Al_{2+2x/3\ x/3}O_4$ Single-Phase Pigment Synthesis and Modification for Electrophoretic Ink Formulation. *ACS Omega* **2020**, *5*, 18651−18661.

(63) Torkian, L.; Daghighi, M. Effects of B-Alanine on Morphology and Optical Properties of $CoAl_2O_4$ Nanopowders as a Blue Pigment. *Adv. Powder Technol* **2014**, *25*, 739−744.

(64) Tangcharoen, T.; T-Thienprasert, J.; Kongmark, C. Effect of Calcination Temperature on Structural and Optical Properties of MAl_2O_4 (M = Ni, Cu, Zn) Aluminate Spinel Nanoparticles. *J. Adv. Ceram.* **2019**, *8*, 352−366.

(65) Chueachot, R.; Nakhowong, R. Synthesis and Optical Properties of Blue Pigment $CoAl_2O_4$ Nanofibers by Electrospinning. *Mater. Lett.* **2020**, *259*, 126904.

(66) Atchuta, S. R.; Sakthivel, S.; Barshilia, H. C. Selective Properties of High-Temperature Stable Spinel Absorber Coatings for Concentrated Solar Thermal Application. *Solar Energy* **2020**, *199*, 453−459.

(67) Tangcharoen, T.; T-Thienprasert, J.; Kongmark, C. Optical Properties and Versatile Photocatalytic Degradation Ability of MAl_2O_4 (M = Ni, Cu, Zn) Aluminate Spinel Nanoparticles. *J. Mater. Sci.: Mater. Electron.* **2018**, *29*, 8995−9006.

(68) Wang, G.; Luo, F.; Cao, K.; Zhang, Y.; Li, J.; Zhao, F.; Chen, R.; Hong, J. Effect of Ni Content of Ni/Γ Al_2O_3 Catalysts Prepared by the Atomic Layer Deposition Method on Co_2 Reforming of Methane. *Energy Technol.* **2019**, *7*, 1800359.

(69) Ustundag, E.; Clausen, B.; Bourke, M. A. M. Neutron Diffraction Study of the Reduction of $NiAl_2O_4$. *Appl. Phys. Lett.* **2000**, *76*, 694−696.

(70) Wang, H. Y.; Ruckenstein, E. Conversion of Methane to Synthesis Gas over Co/Γ-Al_2O_3 by CO_2 and/or O_2. *Catal. Lett.* **2001**, *75*, 13.

(71) Lamouri, S.; Hamidouche, M.; Bouaouadja, N.; Belhouchet, H.; Garnier, V.; Fantozzi, G.; Trelkat, J. F. Control of the Γ-Alumina to A-Alumina Phase Transformation for an Optimized Alumina Densification. *Bol. Soc. Esp. Ceram. Vidrio* **2017**, *56*, 47−54.